International Journal of Mechanical Sciences 151 (2019) 772–784

Contents lists available at ScienceDirect

International Journal of Mechanical Sciences

journal homepage: www.elsevier.com/locate/ijmecsci

Fluid-solid conjugate heat transfer modelling using weakly compressible smoothed particle hydrodynamics

K.C. Ng[a,*], Y.L. Ng[b], T.W.H. Sheu[c], A. Mukhtar[b]

[a] School of Engineering, Taylor's University, Taylor's Lakeside Campus, No. 1, Jalan Taylor's, 47500 Subang Jaya, Selangor Darul Ehsan, Malaysia
[b] Department of Mechanical Engineering, College of Engineering, Universiti Tenaga Nasional (UNITEN), Jalan IKRAM-UNITEN, 43000 Kajang, Selangor Darul Ehsan, Malaysia
[c] Center for Advanced Study on Theoretical Sciences (CASTS), National Taiwan University, Taipei, Taiwan

ARTICLE INFO

Keywords:
Smoothed Particle Hydrodynamics (SPH)
Weakly-compressible
Conjugate Heat Transfer (CHT)
Heat exchanger
Tensile instability
Shifting

ABSTRACT

To date, the Smoothed Particle Hydrodynamics (SPH) method which is mesh-less and fully Lagrangian in nature has been mainly applied in solving solid heat conduction problem and flow convection problem separately. In the current work, we have implemented the Weakly Compressible Smoothed Particle Hydrodynamics (WCSPH) method to solve internal flow problem involving fluid-solid Conjugate Heat Transfer (CHT). In order to ensure heat flux continuity across the interface separating two different materials, the harmonic mean value of thermal conductivities was adopted when modelling the heat transfer between fluid and solid bodies. On the modelling of non-isothermal hydrodynamically fully-developed channel flow, the Dirichlet inlet temperature boundary condition was implemented without having to build a separate temperature reset zone as proposed in the open literature. From the current study, we have found that the particle shifting algorithm is efficient to address the tensile instability problem encountered when simulating flow at high Reynolds number. The WCSPH results were compared against the established analytical and numerical solutions and good agreement was found. The idea of extending the WCSPH method to simulate the flow and heat transfer in parallel-flow and counter-flow heat exchangers was pursued in the current study as well.

1. Introduction

Conjugate Heat Transfer (CHT) happens when fluid flows over a heat-conducting solid body. As such, both interface temperature and heat flux cannot be prescribed beforehand as these properties are dependent on the instantaneous flow and wall properties. Due to the fact that conductive heat transfer in solid body plays a role in the overall heat transfer within the fluid body as well, the conventional boundary conditions such as constant heat flux and constant temperature [1–3] are simply not applicable. In practice, CHT can be found in many engineering applications such as heat exchanger [4], turbine blade cooling [5], electronic cooling [6], etc.

In order to impose the fluid-solid boundary condition for the energy equation in CHT problem, two criteria must be satisfied: (a) temperature and (b) normal heat flux continuities. Depending on how these different domains are coupled, conventional CFD methods can be classified into two groups, i.e. strongly- and weakly-coupled approaches [7]. In general, the weakly-coupled approach is more popular as the existing solvers can be used in simulating CHT problem upon coupling them at the solid-liquid interface. Nevertheless, the implementation of extrapolation and iterative schemes in conventional CFD solver such as that based on the Finite Volume Method (FVM) is necessary in order to satisfy the aforementioned interface boundary condition in CHT problem [8]. This has posed a great challenge to conventional CFD solvers while implementing the fluid-solid boundary condition for problems involving complex interface geometry.

On the other hand, the Lagrangian mesh-less methods (or particle method) such as Smoothed Particle Hydrodynamics (SPH) [9–11], Moving Particle Semi-implicit (MPS) [12–17], Dissipative Particle Dynamics (DPD) [18–20] etc. have been gaining popularity in the simulation study of complex fluid dynamics problems nowadays. In the absence of grid system, the iterative convergence issue in conventional mesh-based method (due to mesh quality) can be effectively resolved using the particle method. According to Liu and Liu [10], SPH is the oldest mesh-less particle method. In fact, SPH has been mainly used in solving free-surface hydrodynamic flow problem as the implementations of dynamic and shear-free boundary conditions at the free surface are straightforward [21]. Unlike the conventional Volume of Fluid (VOF) method, the dynamic tracking of free surface is unnecessary in SPH. Following the pioneering work in simulating free-surface problem using SPH [21], many complex free-surface problems involving splashing, wave breaking and

* Corresponding author.
E-mail addresses: ngkhaiching2000@yahoo.com, khaiching.ng@taylors.edu.my (K.C. Ng).

https://doi.org/10.1016/j.ijmecsci.2018.12.028
Received 18 October 2018; Received in revised form 26 November 2018; Accepted 18 December 2018
Available online 18 December 2018

fragmentation of water-air interface have been simulated [22–24]. In fact, the application of SPH is not limited to only free-surface problem, but also other problems such as those encountered in traffic management [25], microfluidics [26], manufacturing process [27], sport science [28], heat transfer [29], etc.

As compared to free-surface problems involving wave propagation, the number of SPH works in heat transfer simulation is relatively limited in open literature. To date, SPH has been mainly used in modelling convection [30–37], solid conduction [38–40] and solid-liquid phase-change [41–46] problems. Some novel implementations of advanced boundary conditions in non-isothermal flow had been reported as well [47,48]. In fact, the solid-liquid phase-change problem involves CHT between fluid and solid bodies. Although the SPH solutions of solid-liquid phase-change problems had been somehow validated with the experimental data [41,44], we found that the detailed verification of SPH in simulating fluid-solid CHT problem alone has not been presented in open literature so far. On the SPH modelling of heat transfer across the interface of discontinuous thermal conductivity such as that observed in a phase-change problem, the harmonic mean approach initially proposed by Cleary and his co-workers in modelling natural convection [49] and conduction [40] has been commonly used in the discretized SPH equation of energy in order to ensure heat flux continuity across the material interface. By using this formulation, some researchers have successfully simulated the heat conduction problem involving four solid materials using an implicit time integration scheme [50]. More recently, by using this harmonic approach, the heat transfer behavior of fluid flow within a closed cavity containing multiple solid objects had been studied [51]. The temperatures of those solid objects were fixed throughout the course of simulation.

Seemingly, most of the non-isothermal SPH simulations reported above were performed in a closed system. This is mainly due to the difficulties encountered while implementing the inflow and outflow boundary conditions in particle method. Very recently, the heat transfer behavior of nanofluid in a flow channel (with circular obstacle) has been successfully simulated using SPH [29]. The inflow boundary condition was simulated by injecting fluid particles into the problem domain with prescribed velocity and temperature. The outflow boundary condition, on the other hand, was simulated by removing the fluid particles upon exiting the problem domain. Undoubtedly, this approach requires a more complex programming effort. By using the periodic boundary condition on both the inlet and outlet of the flow channel, the CHT problem in a flow channel has been recently simulated using the energy-conserving Dissipative Particle Dynamics (DPD) method [20]. While the velocity field was treated as fully-developed, the flow was thermally developing in the streamwise direction which was realised by fixing the inlet temperature. The Dirichlet temperature boundary condition at the inlet was implemented via placing a temperature reset zone at the upstream region of the channel inlet. That is, the particles exiting the outlet re-enter into the temperature reset zone and their temperatures are reset to the prescribed inlet temperature. Note, the momentum equations are integrated in the temperature reset zone as well. Therefore, extra computational overheads are incurred if the idea of temperature reset zone is pursued.

In the current work, we intend to test the performance of SPH in solving two-dimensional (2D) fluid-solid CHT problem. We focused on the numerical framework of weakly-compressible SPH (WCSPH) method as the pressure field can be updated explicitly without having to solve the Poisson equation of pressure iteratively. Furthermore, the WCSPH code can be effectively parallelized. To the best of the authors' knowledge, extensive verification work in fluid-solid CHT problem using SPH has not been reported so far. For channel flow simulation, we implemented the particle recycling strategy (or periodic boundary condition for hydrodynamic variables) in modelling thermally developing flow in the channel [20]. Nevertheless, unlike their approach, our current implementation does not require the construction of temperature reset zone before executing the simulation. Therefore, our approach should be computationally cheaper than the approach of Zhang and his co-workers [20]. The SPH results were then compared with those simulated from other established method such as Finite Volume Method (FVM) and good agreement has been found. Having establishing the confidence of using SPH in simulating fluid-solid CHT problem, the idea of using SPH in simulating CHT problem such as that encountered in heat exchanger was further pursued in the current work.

2. Mathematical models and numerical method

The fluid physics is governed by mass conservation (continuity):

$$\frac{d\rho}{dt} = -\rho\nabla.\mathbf{v}, \tag{1}$$

momentum conservation:

$$\rho\frac{d\mathbf{v}}{dt} = -\nabla P + \mu\nabla^2\mathbf{v} \tag{2}$$

and energy conservation (without viscous dissipation) equations:

$$\rho\frac{dT}{dt} = \frac{1}{C_p}\nabla.(k\nabla T). \tag{3}$$

In the current work, the heat transfer within the solid region is governed by Eq. (3) as well. All solid bodies were treated as stationary; therefore, the equations of motion Eqs. (1) and ((2)) were not solved for all solid bodies. Here, $\mathbf{v}$ is the fluid velocity vector, P is the fluid pressure, μ is the fluid dynamic viscosity, T is the fluid/solid temperature, ρ is the fluid/solid density, C_p is the fluid/solid specific heat and k is the fluid/solid thermal conductivity. Note, in SPH, the total derivatives (L.H.S of Eqs. (1-3)) are adopted as the flow variables are solved in the fully Lagrangian manner.

3. WCSPH model

3.1. Discretization

The above equations were discretized using the Smoothed Particle Hydrodynamics (SPH) method whereby extensive derivations on the SPH operators have been reported [52]. In the current work, as the fluid was treated as weakly compressible, the fluid pressure P was written as a function of change in fluid density:

$$P = c^2(\rho - \rho_o). \tag{4}$$

Here, c is the speed of sound (10 times the maximum fluid speed in the flow domain) and ρ_o is the initial (reference) fluid density.

By using SPH, the discretized continuity equation of fluid particle i can be written as:

$$\frac{d\rho_i}{dt} = \rho_i\sum_j V_j(\mathbf{v}_i - \mathbf{v}_j)\cdot\nabla_i W_{ij} + 2\delta hc D_i. \tag{5}$$

The summation above takes into account the volume of neighboring particle V_j ($=m_j/\rho_j$), which is robust even when simulating flow with high density ratio such as that encountered in the current fluid-solid CHT problem. The derivative of kernel function $\nabla_i W_{ij}$ is taken with respect to the coordinates of particle i, i.e. $\nabla_i W_{ij} = \frac{dW_{ij}}{dr}.\frac{\mathbf{r}_{ij}}{|\mathbf{r}_{ij}|}$. Here, $\mathbf{r}_{ij}$ denotes $\mathbf{r}_i - \mathbf{r}_j$. The 2nd term in the R.H.S. of Eq. (5) is the density diffusion term introduced to remove the high frequency noise in the pressure field. According to Sun and his co-workers [53], the parameter δ is *not* a tunable parameter and a fixed value of 0.1 can be used for all simulations. In the current work, the smoothing length h was prescribed as 1.0 s, where s is the initial particle spacing. Meanwhile, the quintic spline kernel with compact support radius (r_c) of 3 h was adopted. Therefore, at least 3 layers of dummy particles were placed next to the boundary in order to ensure the full support of kernel interpolation (see Fig. 1). The term D_i can be expressed as:

$$D_i = \sum_j(\rho_j - \rho_i)V_j\frac{\mathbf{r}_{ji}\cdot\nabla_i W_{ij}}{\left\|\mathbf{r}_{ji}\right\|^2}, \tag{6}$$

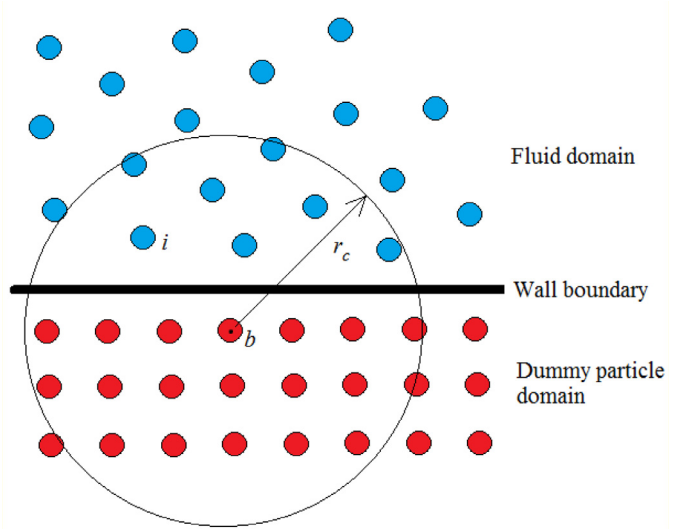

Fig. 1. Extrapolation of pressure at solid/dummy b using the flow information of the neighbouring fluid particle i. r_c is the compact support radius.

In the case of interacting with solid/dummy particles, no density diffusion was applied by simply setting $\rho_j = \rho_i$. Meanwhile, the volume of solid/dummy particles V_j appeared in Equations (5) was fixed ($V_j = s^2$) throughout the simulation.

The acceleration of fluid particle i can be expressed as:

$$\frac{d\mathbf{v}_i}{dt} = -\frac{1}{m_i}\sum_j \left(V_i^2 + V_j^2\right)\frac{P_i\rho_j + P_j\rho_i}{\rho_i + \rho_j}\nabla_i W_{ij} + \frac{1}{m_i}\sum_j \left(V_i^2 + V_j^2\right)\frac{2\mu_i\mu_j}{\mu_i + \mu_j}\frac{\mathbf{v}_i - \mathbf{v}_j}{\left\|\mathbf{r}_{ij}\right\|}\nabla_i W_{ij}\cdot\frac{\mathbf{r}_{ij}}{\left\|\mathbf{r}_{ij}\right\|} \tag{7}$$

Note, the pressures of neighboring solid/dummy particles P_b were extrapolated from the fluid pressure based on the Adami's approach [54] that satisfies momentum balance (see Fig. 1):

$$P_b = \frac{\sum_i \left(P_i - \rho_i \mathbf{a}_b\cdot\mathbf{r}_{bi}\right)W\left(\left\|\mathbf{r}_{bi}\right\|\right)}{\sum_i W\left(\left\|\mathbf{r}_{bi}\right\|\right)} \tag{8}$$

Here, $\mathbf{a}_b = 0$ as the boundaries and solid bodies were treated as stationary. The densities of neighboring solid/dummy particles ρ_b were calculated from P_b based on the state equation (Eq. (4)). The volume of neighboring solid/dummy particles V_b was then computed as $V_b = m_i/\rho_b$, where m_i is the mass of the approaching fluid particle i. In order to impose the no-slip wall boundary condition, the velocity of solid/dummy particle b can be approximated by taking into account the prescribed solid/dummy velocity $\mathbf{v}_w$ [54]:

$$\mathbf{v}_b = 2\mathbf{v}_w - \frac{\sum_{j\in N_f}\mathbf{v}_j W\left(\left\|\mathbf{r}_{bj}\right\|\right)}{\sum_{j\in N_f} W\left(\left\|\mathbf{r}_{bj}\right\|\right)}, \tag{9}$$

where N_f is the number of neighbouring fluid particles. This method is attractive as the boundary surface normal information is not required. Note, the summation term on the R.H.S. of Eq. (9) indicates that the local fluid velocity is extrapolated to the position of solid/dummy particle b.

Finally, the discretized energy equation for both fluid and solid bodies can be written as:

$$\frac{dT_i}{dt} = \frac{1}{\rho_i C_p}\sum_j V_j \frac{4k_i k_j}{k_i + k_j}\frac{\mathbf{r}_{ij}\cdot\nabla_i W_{ij}}{\left(\left\|\mathbf{r}_{ij}\right\|^2 + 0.01h^2\right)}\left(T_i - T_j\right) \tag{10}$$

By using the harmonic mean of thermal conductivities, the above formulation is readily applicable for computing the heat flux between materials of different thermal conductivities [40]. In the current study, the Dirichlet boundary condition was imposed by calculating the temperature of dummy particle based on Eq. (9) upon replacing $\mathbf{v}$ with T. The dummy particles are skipped (i.e. $T_i = T_j$ in Eq. (10)) if the boundary is adiabatic.

The velocity-Verlet scheme was used to integrate the differential equations in time:

$$\mathbf{v}_i^{\,n+\frac{1}{2}} = \mathbf{v}_i^{\,n} + \frac{\Delta t}{2}\left(\frac{d\mathbf{v}_i}{dt}\right)^n \tag{11}$$

$$\mathbf{r}_i^{\,n+\frac{1}{2}} = \mathbf{r}_i^{\,n} + \frac{\Delta t}{2}\mathbf{v}_i^{\,n+\frac{1}{2}} \tag{12}$$

$$T_i^{\,n+\frac{1}{2}} = T_i^{\,n} + \frac{\Delta t}{2}\left(\frac{dT_i}{dt}\right)^n \tag{13}$$

$$\rho_i^{\,n+1} = \rho_i^{\,n} + \Delta t\left(\frac{d\rho_i}{dt}\right)^{n+\frac{1}{2}} \tag{14}$$

$$\mathbf{r}_i^{\,n+1} = \mathbf{r}_i^{\,n+\frac{1}{2}} + \frac{\Delta t}{2}\mathbf{v}_i^{\,n+\frac{1}{2}} \tag{15}$$

$$\mathbf{v}_i^{\,n+1} = \mathbf{v}_i^{\,n+\frac{1}{2}} + \frac{\Delta t}{2}\left(\frac{d\mathbf{v}_i}{dt}\right)^{n+1} \tag{16}$$

$$T_i^{\,n+1} = T_i^{\,n+\frac{1}{2}} + \frac{\Delta t}{2}\left(\frac{dT_i}{dt}\right)^{n+1} \tag{17}$$

Here, the superscript n denotes the time level. Due to the nature of the fully explicit time integration scheme implemented in the current work, the time step size, Δt was restricted in the following manner for stability purpose:

$$\Delta t = \min\left(0.125\frac{\rho_o h^2}{\mu}, 0.25\sqrt{\frac{h}{\left\|\mathrm{a_i}\right\|_{max}}}, 0.25\frac{h}{c}, 0.5\frac{\rho_s C_{p,s} h^2}{k_s}\right), \tag{18}$$

where $\|\mathbf{a}_i\|_{max}$ is the maximum acceleration in the flow field and the subscript s denotes solid body.

The positions of fluid particles were updated according to Eq. (15). Nevertheless, as demonstrated in our test case later, we noticed that the SPH solution became unstable in regions characterized by large flow gradient (e.g. in the near-wall boundary layer). The particles within this region became highly anisotropic and their spatial configurations were non-uniform. In fact, this phenomenon is more noticeable at higher Reynolds number. In order to regularize the positions of SPH fluid particles, the use of shifting method is relatively popular [55,56] as compared to other methods such as constant background pressure [57] and artificial pressure [58]. In the current work, we implemented the shifting algorithm reported in the recent δ-plus SPH method [53]:

$$\mathbf{r}_i^{\,n+1,*} = \mathbf{r}_i^{\,n+1} + \boldsymbol{\delta}\mathbf{r}_i^{\,n+1}, \tag{19}$$

where $\mathbf{r}_i^{\,n+1,\,*}$ is the shifted particle position and $\boldsymbol{\delta}\mathbf{r}_i^{\,n+1}$ is the displacement vector defined as:

$$\boldsymbol{\delta}\mathbf{r}_i^{\,n+1} = -2ch\left|\mathbf{u}_{max}\right|\sum_j\left[1 + R\left(\frac{W\left(\left\|\mathbf{r}_{ij}\right\|\right)}{W(s)}\right)^n\right]\nabla_i W_{ij}V_j \tag{20}$$

It is noted that the term $R(\frac{W(\|\mathbf{r}_{ij}\|)}{W(s)})^n$is inherited from the artificial pressure formulation [58]. Here, if the neighbouring particle is a fluid particle, V_j is defined as the averaged fluid volume: $V_j = 2m_j/(\rho_i + \rho_j)$ introduced to ensure momentum conservation [53]. Otherwise, $V_j = s^2$. Following the original work of artificial pressure [58], R and n were set to 0.2 and 4, respectively. As reported in the δ-plus SPH method, the above shifting algorithm is not very sensitive to the specific choices of R and n. In the current work, we did not interpolate the flow variables onto the new (or shifted) particle positions as the effect had been found to be small [59].

In short, the current numerical procedure can be summarized as:

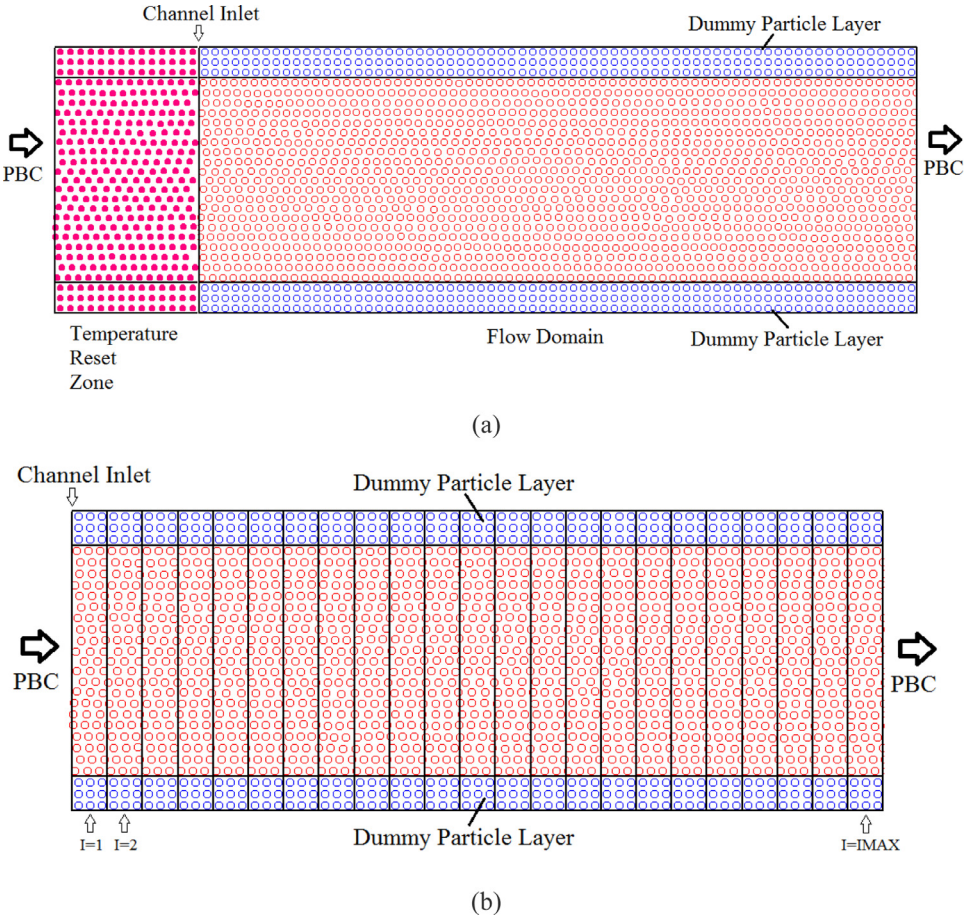

Fig. 2. Handling of inlet Dirichlet boundary condition. (a) Temperature reset zone [20] established at the upstream region of the channel inlet is used to reset the temperatures of particles that re-enter through the channel inlet. (b) Our current approach without using temperature reset zone. I is the index of the background cell in the x-direction.

Step 1: From the current time level n, compute the velocities and positions of SPH fluid particles at the intermediate time level $n+\frac{1}{2}$ using Eqs. (11) and (12), respectively.

Step 2: Compute the temperatures of SPH fluid and solid particles at the intermediate time level $n+\frac{1}{2}$ using Eq. (13).

Step 3: Update the densities of SPH fluid particles at new time level $n+1$ using Eq. (14). Based on the updated density values, obtain the pressures of SPH fluid particles using Eq. (4).

Step 4: Update the positions of SPH fluid particles at new time level $n+1$ using Eq. (15).

Step 5: By using the updated positions from Step 4, compute the velocities of SPH fluid particles at new time level $n+1$ using Eq. (16).

Step 6: Compute the temperatures of SPH fluid and solid particles at new time level $n+1$ using Eq. (17).

Step 7: Reposition the SPH fluid particles using the shifting algorithm outlined in Eq. (19).

Step 8: Repeat Step 1 to Step 7 until the desired time level is reached.

3.2. Handling of isothermal inlet boundary condition in a hydrodynamically fully-developed channel

For simulating a hydrodynamically fully-developed flow in a channel, one may resort to applying the periodic boundary condition for the hydrodynamic variables in the streamwise direction. However, for non-isothermal problem, as the temperature varies along the streamwise direction due to the heat exchange between the fluid and the non-adiabatic channel wall, the use of periodic boundary condition is improper for the temperature variable. In order to resolve this issue, the temperature reset zone has been placed at the upstream region of the channel flow inlet [20]. While recycling those exiting particles back to the problem domain, those particles are forced to pass through the temperature reset zone so that their temperatures are reset to the desired inlet temperature (T_{inlet}). The idea is illustrated in Fig. 2(a). Here, no heat exchange was allowed between the particles in the temperature reset zone and those in the channel flow domain to avoid heat diffusion between these two zones.

Following the above approach of Zhang and his co-workers [20], the temperature reset zone must be built before a simulation is started. Since the momentum and continuity equations are solved for particles within the temperature reset zone as well, this would impose additional computational overhead on the SPH flow solver. In the current work, we found that it was unnecessary to construct the temperature reset zone. Since we have established the background cells for particle searching purpose, we kept the lists of particles that lie adjacent to the periodic faces ($I=1$ and $I=$NMAX). As shown in Fig. 2(b), if a particle from $I=1$ interacts with that from $I=$NMAX, the neighbouring temperature of particle at $I=$NMAX is fixed at the desired inlet temperature (i.e. setting $T_j=T_{inlet}$ in Eq. (10)). In the current work, we still rely on the particle recycling strategy in simulating the hydrodynamically fully-developed flow. Once the exiting particles re-enter the flow domain from the inlet boundary, their inlet temperatures are modified to become T_{inlet}. This extra treatment would enable us to simulate the heat diffusion from an isothermal inlet without having to build an external temperature reset zone. This idea is verified in the next section.

4. Results and discussions

In order to test our implementation of our non-isothermal SPH solver, we have simulated a series of test cases before venturing into solving the more complex fluid-solid conjugate heat transfer problem. Firstly, we tested our present SPH solver in simulating the unsteady heat

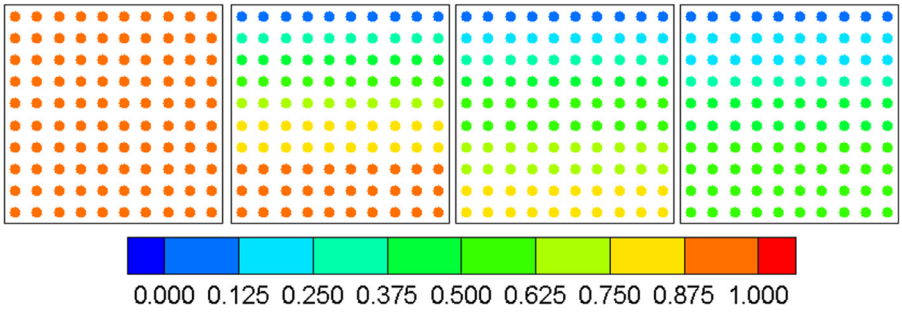

Fig. 3. Dimensionless particle temperature ($T^* = (T\text{-}T_C)/(T_H\text{-}T_C)$) at $t = 0$ s, 40 s, 80 s and 180 s (from left to right). $T_H = 200$ °C and $T_C = 0$ °C.

conduction in a homogeneous solid body. Next, we tested the capability of Eq. (10) in handling heat transfer within multiple solid bodies made from different materials. The idea of simulating the heat diffusion from an isothermal inlet was then tested by simulating the non-isothermal Poiseuille flow in a flow channel. The temperatures of the channel walls were fixed. Having verified the implementation of isothermal inlet temperature boundary condition, the fluid-solid conjugate heat transfer problem was simulated and the result was verified with the more established finite volume solution obtained from ANSYS FLUENT. Finally, the current method was used to simulate the heat transfer processes in the parallel-flow and counter-flow heat exchangers.

4.1. Transient heat conduction in a homogeneous solid

In this section, we intend to simulate the transient heat conduction problem in a solid body. At $t = 0$ s, the temperature of the square domain of length $L = 2$ cm was $T_H = 200$ °C. The temperature of the upper wall was then abruptly decreased to $T_C = 0$ °C at $t > 0$ s and meanwhile the lower wall was set as adiabatic. The left and right boundaries were periodic. A total of 10×10 SPH particles were used to simulate this simple heat conduction problem and the result was then compared against the analytical temperature solution [°C]:

$$T(y,t) = \frac{-800}{\pi} \sum_{n=1}^{\infty} \frac{(-1)^{n+1}}{2n-1} \exp\left(-\frac{k}{\rho C_p} \lambda_n^2 t\right) \cos\left(\lambda_n y\right) \tag{21}$$

where $\lambda_n = \frac{2n-1}{2L}\pi$. The density, thermal conductivity and heat capacity terms appeared in the above equation were set as $\rho = 1.0$ kgm^{-3}, $k = 10$ Wm^{-1}K^{-1} and $C_p = 1 \times 10^7$ Jkg^{-1}K^{-1}, respectively.

Fig. 3 shows the distributions of dimensionless particle temperature ($T^* = (T\text{-}T_C)/(T_H\text{-}T_C)$) at different time levels. The decrease of solid temperature is evident during the entire cooling process. In order to verify the current SPH implementation, we have compared our simulated dimensionless temperatures along the y-direction against the analytical solutions at different time levels as shown in Fig. 4. A very good agreement has been found.

4.2. Heat conduction in multiple solids

Next, we intend to solve the heat conduction problem in multiple solid bodies. Here, the problem domain of size 4 m x 1 m consisting of three solid bodies (see Fig. 5) was considered. The sizes of the right and left solid bodies were identical (i.e. 1 m x 1 m). Several thermophysical properties of these three solid bodies such as density and heat capacity were assumed to be similar: $\rho = 1.0$ kgm^{-3}, and $C_p = 1 \times 10^3$ Jkg^{-1}K^{-1}. Nevertheless, the thermal conductivity of the middle solid body was prescribed as $k = 2$ Wm^{-1}K^{-1}, which was 5 times lower than those of the other solid bodies. The total number of solid particles was 1600 ($s = 0.05$ m).

In order to simulate the 1D heat conduction, the top and bottom boundaries were treated as periodic. The right and left wall temperatures were set to $T_H = 420$ K and $T_C = 300$ K, respectively. The initial temperatures of the solid bodies were set to T_C and the simulation was

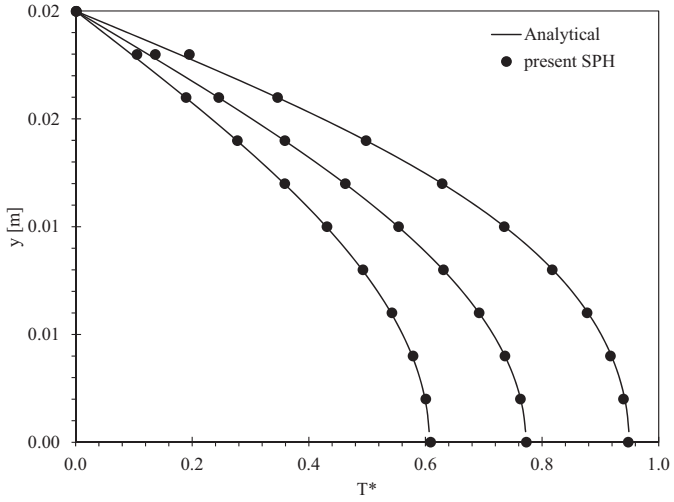

Fig. 4. Distributions of dimensionless temperature ($T^* = (T\text{-}T_C)/(T_H\text{-}T_C)$) along the y-direction at $t = 40$ s, 80 s and 120 s. $T_H = 200$ °C and $T_C = 0$ °C. Temperature drops with respect to time.

carried out until the steady-state condition was achieved ($t = 2000$ s). Fig. 5 shows the distribution of dimensionless particle temperature ($T^* = (T\text{-}T_C)/(T_H\text{-}T_C)$) at steady-state condition. As seen, the temperature contrasts in solid bodies of higher thermal conductivity (i.e. left and right solid bodies) are less evident than that of lower thermal conductivity (middle solid), revealing the fact that heat can be travelled more easily in material of higher thermal conductivity. The numerical solutions of temperature were compared against the theoretical solutions in Fig. 6 and good agreement has been found.

4.3. Transient poiseuille flow

In this Section, we intend to verify our present non-isothermal SPH solver by simulating the Poiseuille flow problem involving heat transfer. This problem had been previously simulated using the energy-conserving DPD particle method [20]. In particular, the 2D rectangular flow channel of size 200 m x 20 m was considered. In this problem, the lower left corner of the flow channel was treated as the origin (0 m, 0 m). The size of SPH fluid particle was set to 1.0 m (i.e. 4000 fluid particles inside the flow domain). The following fluid properties were considered: $\mu = 0.248$ Nsm^{-2}, $\rho = 1.00$ kgm^{-3}, $k = 131{,}914.89$ Wm^{-1}K^{-1} and $C_p = 1 \times 10^5$ Jkg^{-1}K^{-1}. The fluid was subjected to an external acceleration $f_x = 8u_{max}\mu/(\rho W^2)$, where W is the channel width ($W = 20$ m). By setting the maximum x-velocity u_{max} as 8.08 ms^{-1}, the flow Reynolds number is $Re = \rho u_{max} W/\mu = 652$. For the velocity boundary condition, the left and right boundaries were set as periodic while the top and bottom boundaries were treated as no-slip walls. On the other hand, for the temperature boundary condition, the top and bottom boundaries were set as isothermal ($T = 420$ K), while the outflow (right) boundary

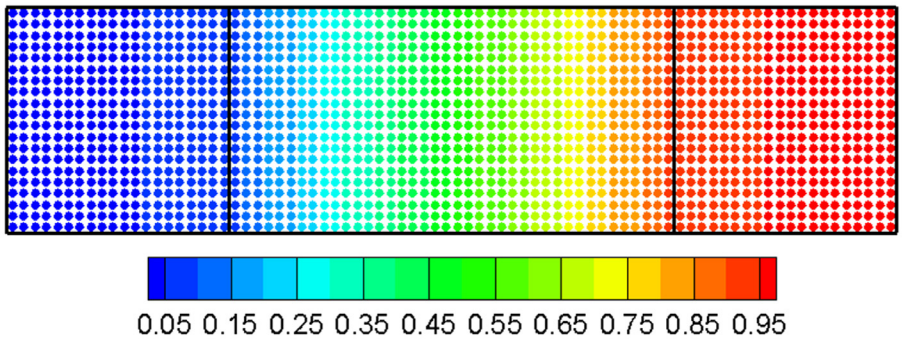

Fig. 5. Steady-state particle dimensionless temperature distribution ($T^* = (T\text{-}T_C)/(T_H\text{-}T_C)$) for multi-solid heat conduction problem. $T_H = 420$ K and $T_C = 300$ K.

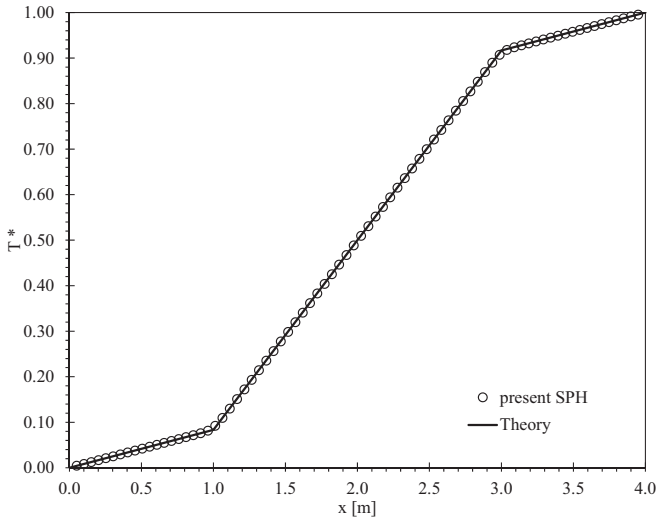

Fig. 6. Changes of dimensionless temperature ($T^* = (T\text{-}T_C)/(T_H\text{-}T_C)$) along the x-direction for multi-solid heat conduction problem. $T_H = 420$ K and $T_C = 300$ K.

was treated as adiabatic. The temperature of the inflow (left) boundary, however, was fixed at $T_o = 300$ K. Meaning to say, when the recycling strategy was implemented to relocate the exiting particles into the flow domain through the inlet boundary, the temperature of this relocated particle was reset to T_o. The simulation was executed until $t = 2000$ s to ensure that the steady-state condition was achieved.

In fact, the long-term simulation of Poiseuille flow problem has posed a significant numerical challenge for standard SPH (SSPH) at high Reynolds number. At the current Re, we found that the flow was initially stable whereby the fluid particles moved in an ordered row fashion. Nevertheless, as time progresses, some agitations in the spanwise (or vertical) velocity field were noticeable near the wall region and these agitations would ultimately spoil the laminar flow structure as seen in Fig. 7 at $t > 150$ s. This observation is agreeable with that reported by [60], and they have highlighted that the agitated flow near the wall would spread into the inner flow region. More recently, Meister and his co-workers [61] have experienced the same instability problem and they found that the steady-state laminar flow state can only be attained if $Re < 65$. In order to defer the instability to higher Re, they reported that additional numerical treatment such as spanwise velocity suppression could be employed. Unfortunately, this treatment could not prevent the break-up of smooth laminar structure from occurring. In the current work, we implemented the shifting algorithm (Eq. (19)) and it was found that the laminar structure remained stable at $t = 2000$ s (steady-state condition) as shown in Fig. 8. Fig. 9 shows the spanwise velocity distributions in the y-direction upon activating the shifting algorithm. As seen, the spanwise velocity is significantly lesser than that of the standard SPH (SSPH) method. Meanwhile, the mid-stream x-velocity converges to the theoretical solution as demonstrated in Fig. 10.

Fig. 11 shows the steady-state temperature and x-velocity distributions. The uniform velocity profile is evident in the anticipated fully-developed flow condition. Due to the presence of heated walls, the fluid temperature increases monotonically along the streamwise direction.

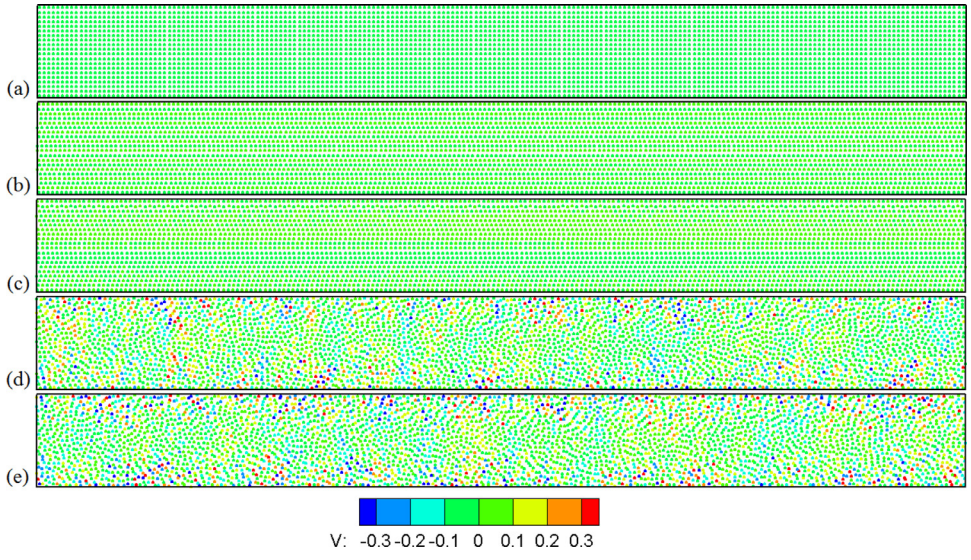

Fig. 7. Time evolutions of particle v-velocity for Poiseuille flow problem ($Re = 652$) at (a) $t = 0$ s, (b) $t = 50$ s, (c) $t = 100$ s, (d) $t = 150$ s and (e) $t = 2000$ s. Standard SPH (SSPH) with no particle shifting is used.

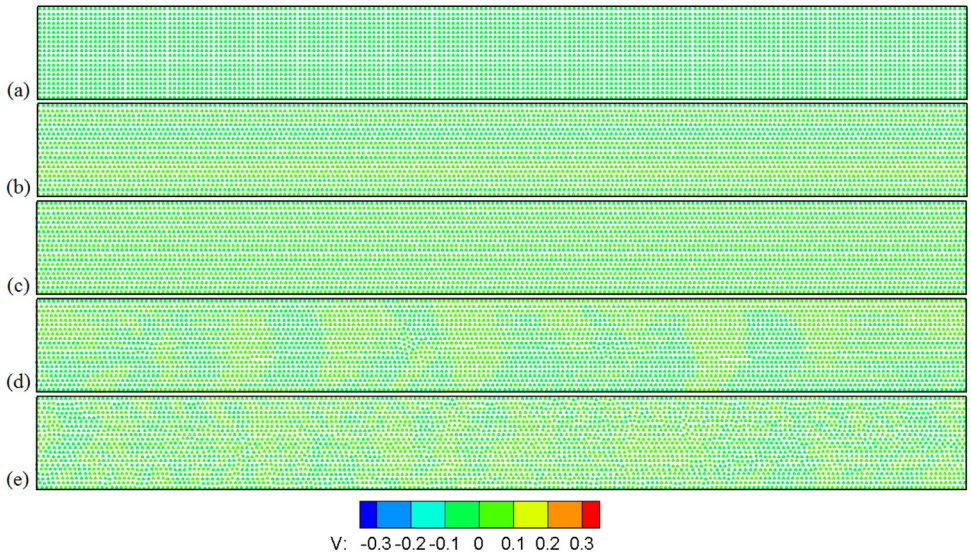

Fig. 8. Time evolutions of particle v-velocity for Poiseuille flow problem ($Re = 652$) at (a) $t = 0$ s, (b) $t = 50$ s, (c) $t = 100$ s, (d) $t = 150$ s and (e) $t = 2000$ s. Present SPH with particle shifting is applied.

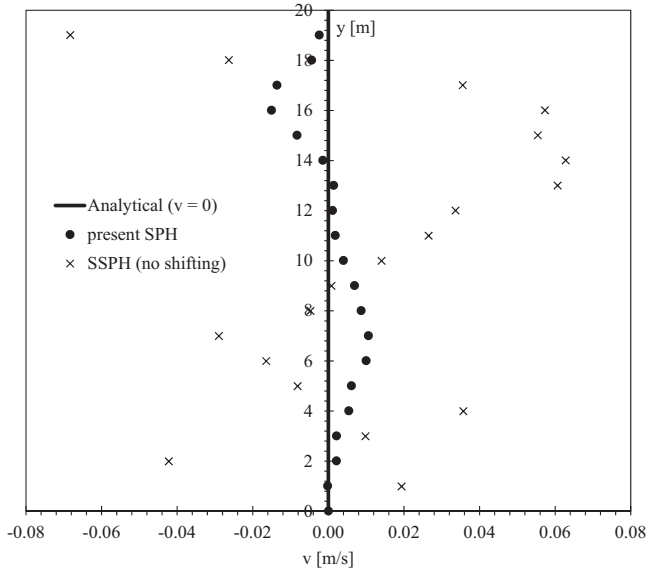

Fig. 9. The y-velocity (v) profiles for Poiseuille flow problem ($Re = 652$) at $t = 2000$ s.

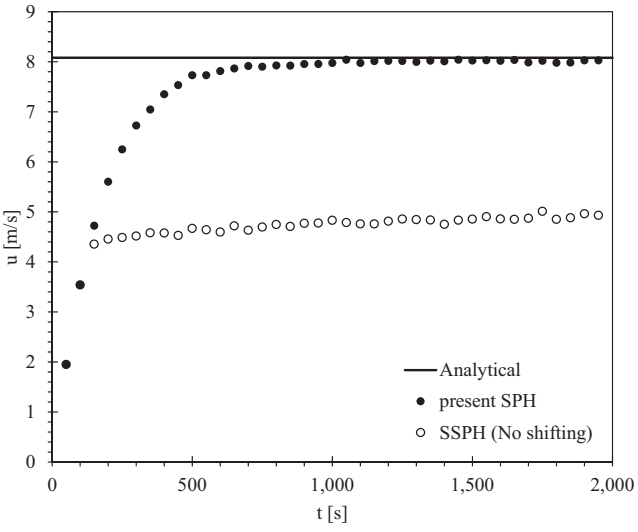

Fig. 10. Comparison of x-velocities at the centroid of the flow channel.

Seemingly, the thickness of the thermal boundary layer grows along the flow direction as well. Therefore, it is anticipated that the heat transfer rate is more intense near the inlet region where the thickness of the thermal boundary layer is the minimum (highest temperature gradient). In order to verify the current implementation, we have compared the x-velocity distributions with the analytical solutions at different time levels and good agreement has been found as outlined in Fig. 12. The discrepancies between the SSPH and the analytical solutions is evident at $t \geq 200$ s. We have also compared the simulated temperature profiles at different flow sections spanning from $x = 5$ m to $x = 195$ m with those of the high-resolution Finite Volume Method (FVM) (MUSCL scheme in ANSYS FLUENT) as shown in Fig. 13. Again, the agreement is promising. As seen from Fig. 13, the near-wall temperature gradient decreases as the flow travels downstream, due to the thickening of thermal boundary layer.

4.4. Fluid-Solid conjugate heat transfer in thick-wall flow channel

This test case is similar to the one discussed earlier in Section 4.3, except that the upper and lower walls were replaced by two thick heat-conducting solid bodies. The size of the solid body was 200 m x 10 m. The fluid properties were similar to those of the previous case, i.e. $\mu = 0.248$ Nsm^{-2}, $\rho = 1.00$ kgm^{-3}, $k = 131{,}914.89$ Wm^{-1}K^{-1} and $C_p = 1 \times 10^5$ Jkg^{-1}K^{-1}. For the solid bodies, the thermophysical properties were similar to those of the fluid body except that the solid thermal conductivity k_s could be increased up to $5k$ at certain simulation conditions. Here, the subscript s denotes the solid body.

Similar to the previous test case, the simulation was executed until $t = 2000$ s in order to attain the steady-state condition. Fig. 14 shows the steady-state x-velocity distribution within the flow channel. The flow enters the flow domain through the left boundary at the inlet temperature of $T_o = 300$ K. Here, it is important to note that the solid particles were stationary during the simulation, except that the extrapolated velocity vectors were assigned onto the solid particles adjacent to the fluid-solid interface during the viscous force calculation. Also, the pres-

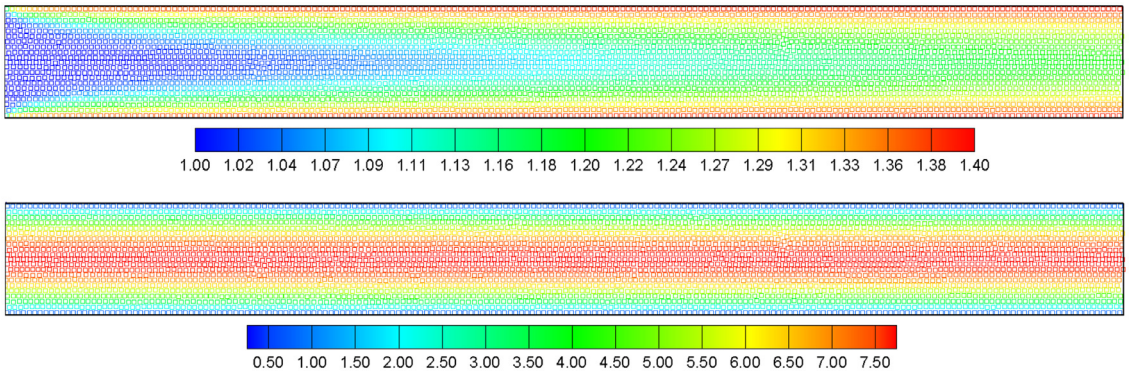

Fig. 11. Steady-state dimensionless temperature T/T_o (top) and x-velocity [m/s] (bottom) distributions of non-isothermal Poiseuille flow problem. $T_o = 300$ K.

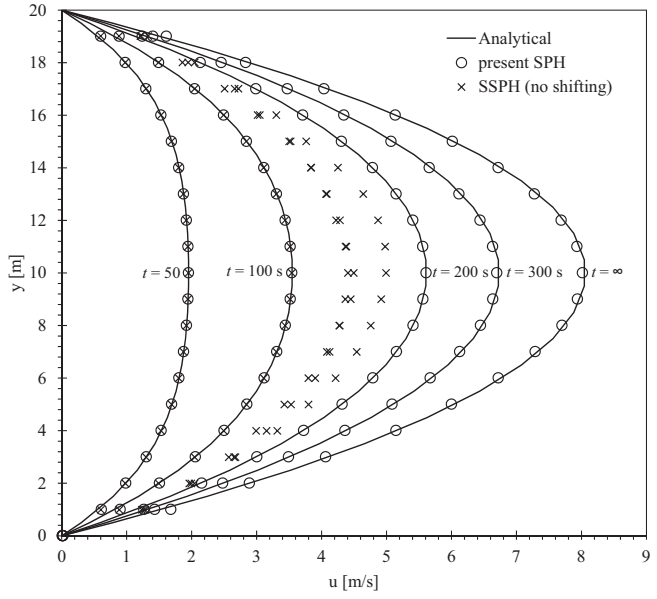

Fig. 12. Transient development of velocity profiles ($t = 50$ s, 100 s, 200 s, 300 s, ∞) for the non-isothermal Poiseuille flow problem. $Re = 652$.

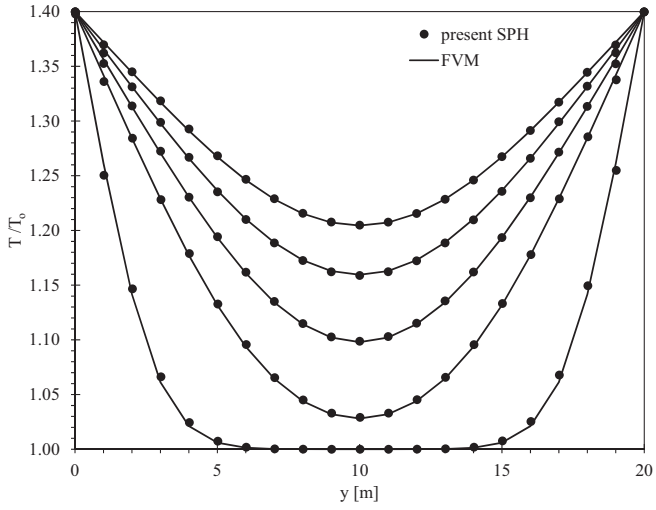

Fig. 13. Steady-state dimensionless temperature distributions at $x = 5$ m, 50 m, 100 m, 150 m and 195 m. Temperature increases along the downstream direction. $Re = 652$ and $T_o = 300$ K.

sures of these solid particles were updated according to the approach outlined in Eq. (8).

Firstly, we made a qualitative comparison between the results obtained from SPH and FVM methods for two different Reynolds numbers: $Re = 65.2$ (Figs. 15 and 16) and $Re = 652$ (Figs. 17 and 18). The flow Reynolds number was adjusted by simply manipulating the external acceleration f_x imposed on the fluid particles. For all the test cases considered here, the top and bottom edges of the problem domain were isothermal: $T = 420$ K. The left and right edges of the solid bodies, however, were treated as adiabatic. As the solid temperature was essentially higher than the incoming fluid temperature ($T_o = 300$ K), the fluid underwent heating operation and thus the temperature increased along the streamwise direction. As expected, as the solid thermal conductiv-

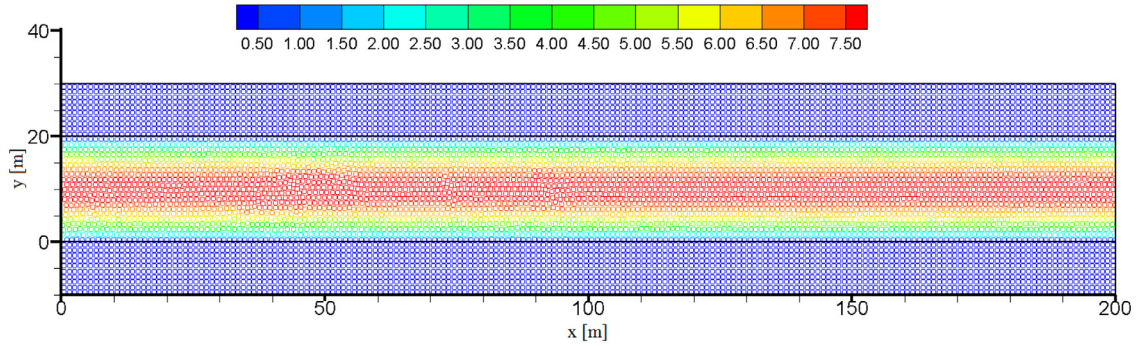

Fig. 14. Geometry layout and steady-state x-velocity (u) distribution [m/s] in the thick-wall flow channel. The top and bottom rectangular regions indicate the stationary heat-conducting solid bodies.

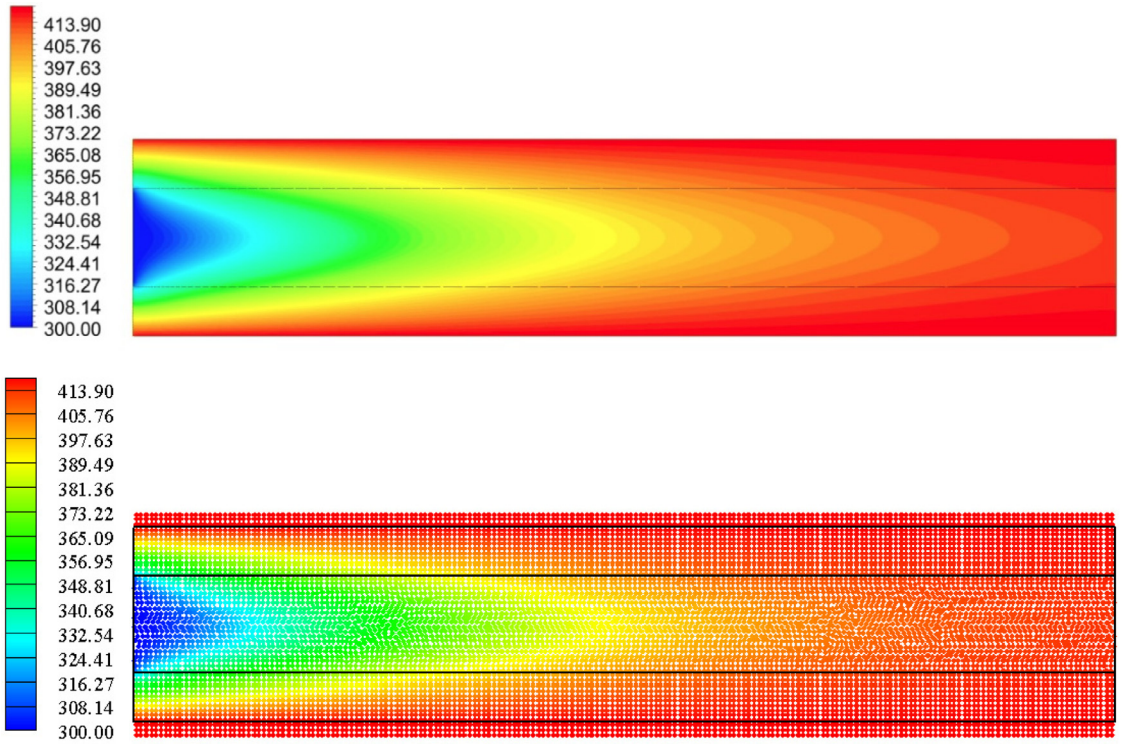

Fig. 15. Comparison of temperature distribution [K] in the thick wall flow channel. $Re = 65.2$ and $k_s/k = 1$. Top: FVM (ANSYS FLUENT); Bottom: present SPH.

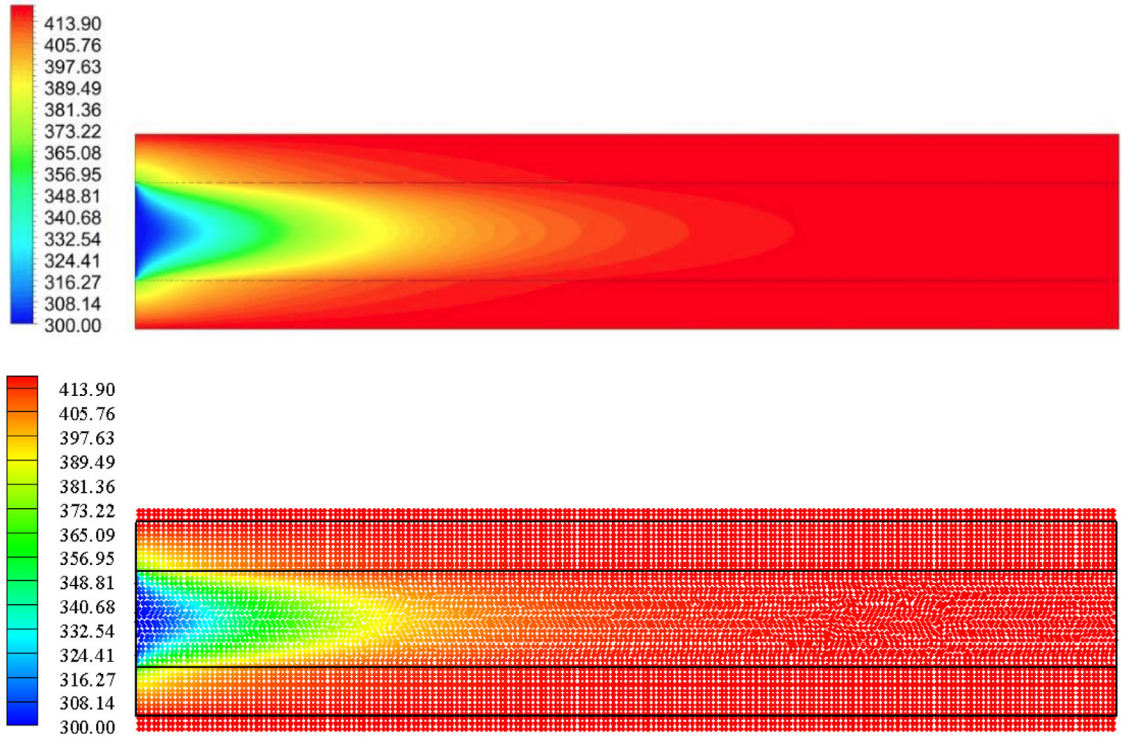

Fig. 16. Comparison of temperature distribution [K] in the thick wall flow channel. $Re = 65.2$ and $k_s/k = 5$. Top: FVM (ANSYS FLUENT); Bottom: present SPH.

ity increases ($k_s/k = 5$), the heating effect is more pronounced and the outlet fluid temperature is higher (see Figs. 16 and 18). Nevertheless, the outlet fluid temperature drops as the *Re* increases, as the convective effect of the incoming cold particles is now more dominant. All in all, the temperature distributions predicted by using SPH are comparable to those of FVM.

Next, the spanwise variations of temperature at different flow sections: $x = 50$ m, 100 m and 150 m predicted using SPH and FVM were compared. At $Re = 65.2$ (see Fig. 19), the overall temperature solution for SPH is not sensitive to the particle resolution as long as the particle size s is below 2.0 m. Note, for the case of $Re = 652$ (see Fig. 20), it was found that the particle resolution should be set to at least $s < 1.429$ m

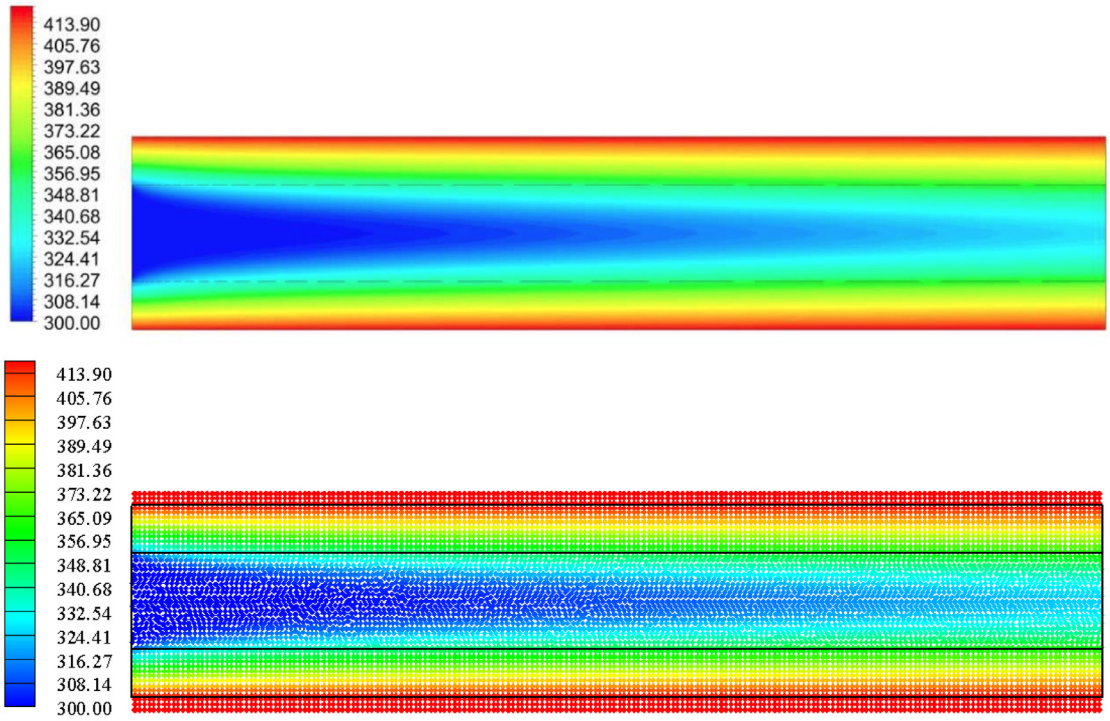

Fig. 17. Comparison of temperature distribution [K] in the thick wall flow channel. $Re = 652$ and $k_s/k = 1$. Top: FVM (ANSYS FLUENT); Bottom: present SPH.

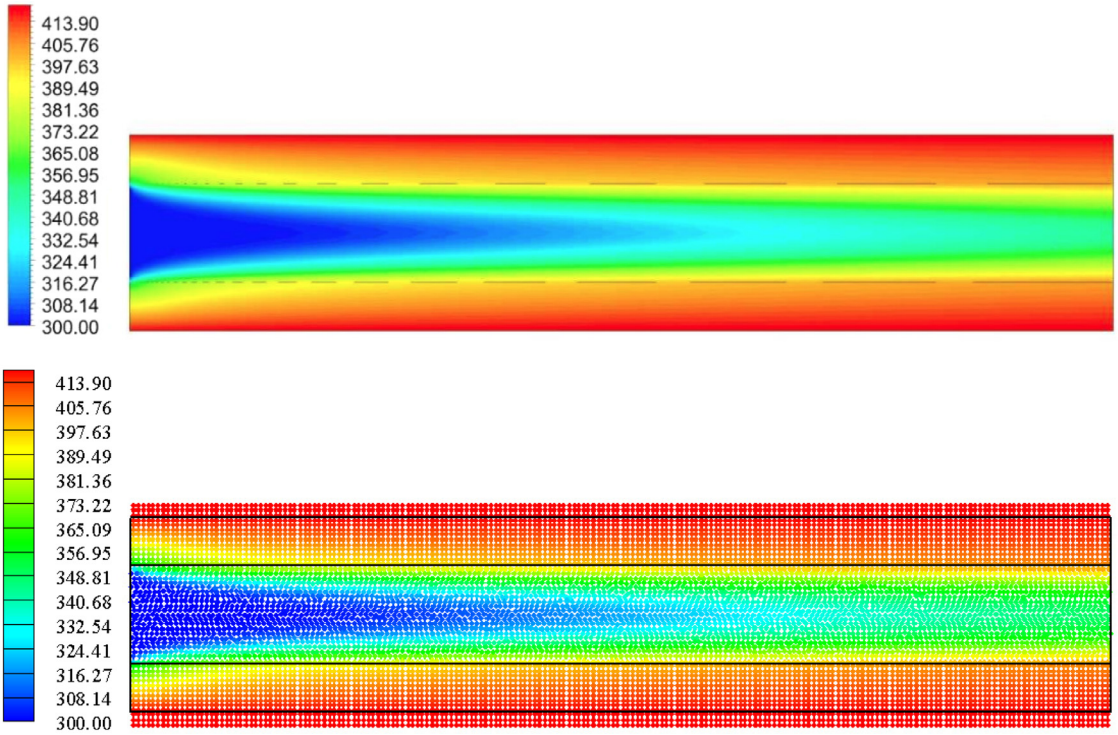

Fig. 18. Comparison of temperature distribution [K] in the thick wall flow channel. $Re = 652$ and $k_s/k = 5$. Top: FVM (ANSYS FLUENT); Bottom: present SPH.

in order to avoid numerical instability from occurring (unphysical spanwise velocity agitation near the wall). As shown in Figs. 19 and 20(b), the sensitivity of particle resolution on the temperature result is somewhat more pronounced near the fluid-solid interface when $k_s/k = 5$, which is partly due to the abrupt change of temperature gradient near the interface and the smoothing effect when post-processing the SPH results on the fixed mesh layout. Overall, the agreement between SPH and finite volume solutions is promising.

4.5. Counter-Flow and parallel-flow heat exchangers

Lastly, we applied the SPH method in simulating the heat exchange between two flow streams separated by a solid heat conductor. Fig. 21

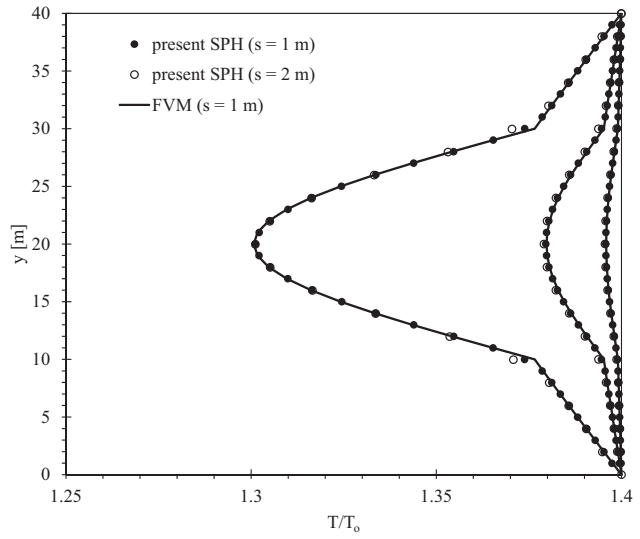

Fig. 19. Steady-state temperature distributions at $x = 50$ m, 100 m and 150 m for $k_s/k = 5$. $Re = 65.2$ and $T_o = 300$ K. Temperature increases along the x- direction.

shows the geometrical layout of a typical counter-flow heat exchanger. The sizes of the flow channels and solid heat conductor were 2.0 m x 0.1 m. The particle size was set as $s = 0.01$ m. For this problem, the fluid properties are $\mu = 0.15$ Nsm^{-2}, $\rho = 1000.00$ kgm^{-3}, $k = 10.00$ Wm^{-1}K^{-1} and $C_p = 25.00$ Jkg^{-1}K^{-1}. For the solid heat conductor, $\rho_s = 8000.00$ kgm^{-3}, $k_s = 50.00$ Wm^{-1}K^{-1} and $C_{p,s} = 500.00$ Jkg^{-1}K^{-1}. The fluid particles at the bottom (cold) and top (hot) flow channels were driven by an external force of $f_x = \pm 0.012$ ms^{-2} and $f_x = 0.024$ ms^{-2}, respectively. Note, the external force acting on the particles in the bottom (cold) flow channel was reversed when modelling the counter-flow heat exchanger as seen in Fig. 21. The inlet temperatures of the hot and cold flow streams were $T_H = 800$ K and $T_C = 300$ K, respectively. The simulation was carried out until $t = 2000$ s.

Fig. 22 shows the dimensionless temperature distributions ($T^* = (T\text{-}T_C)/(T_H\text{-}T_C)$) within the counter-flow and parallel-flow heat exchangers. As seen, the fluid particles in the bottom flow channel constantly pick up the heat conducted from the upper hot streams and hence the fluid temperature increases along the streamwise direction. Meanwhile, the heat loss occurred within upper hot stream is manifested by its decreasing temperature pattern along the streamwise direction. Fig. 23 shows the temperature patterns along the centrelines of the flow channels. It is evident that the outlet temperature of the bottom (cold) flow stream for the counter-flow heat exchanger is higher than that for the parallel-flow heat exchanger, showing that the heat transfer efficiency of counter-flow heat exchanger is indeed better.

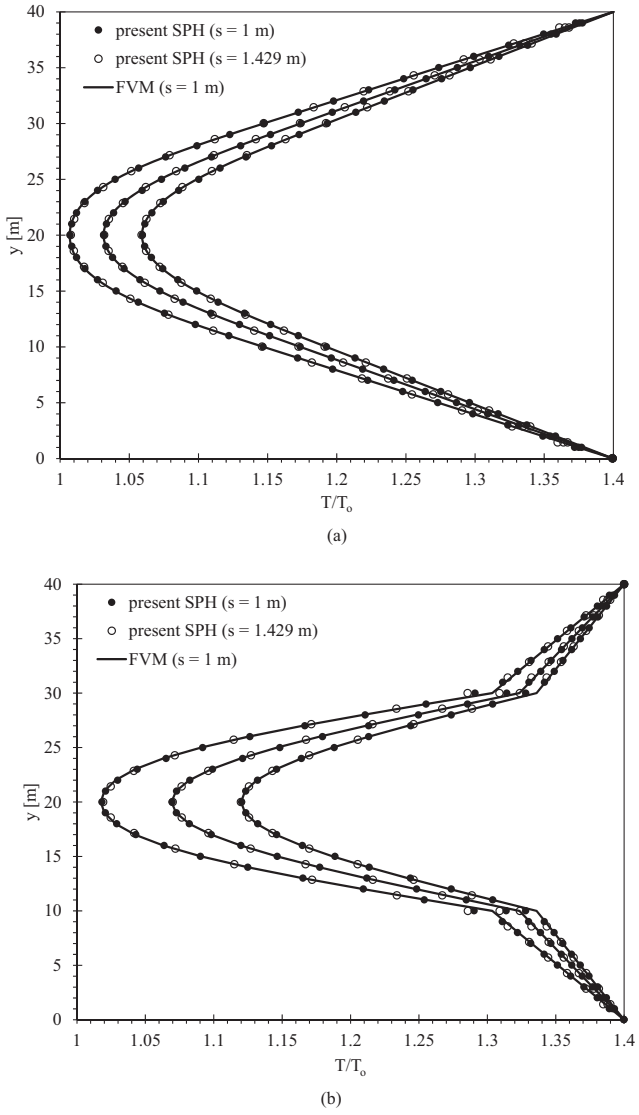

Fig. 20. Steady-state temperature distributions at $x = 50$ m, 100 m and 150 m for (a) $k_s/k = 1$ and (b) $k_s/k = 5$. $Re = 652$ and $T_o = 300$ K. Temperature increases along the x- direction.

5. Conclusion

In this paper, a weakly-compressible SPH solver has been developed to simulate fluid-solid Conjugate Heat Transfer (CHT) problem. In order to resolve the heat flux continuity across the interface separating

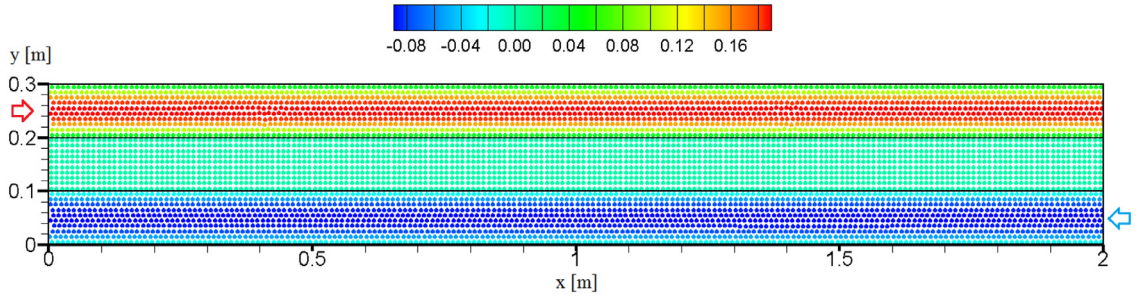

Fig. 21. Geometry layout and x-velocity (u) distribution [m/s] at $t = 2000$ s for the counter-flow heat exchanger. Red and blue arrows indicate hot and cold flow inlets, respectively. The middle rectangular region indicates heat-conducting solid body.

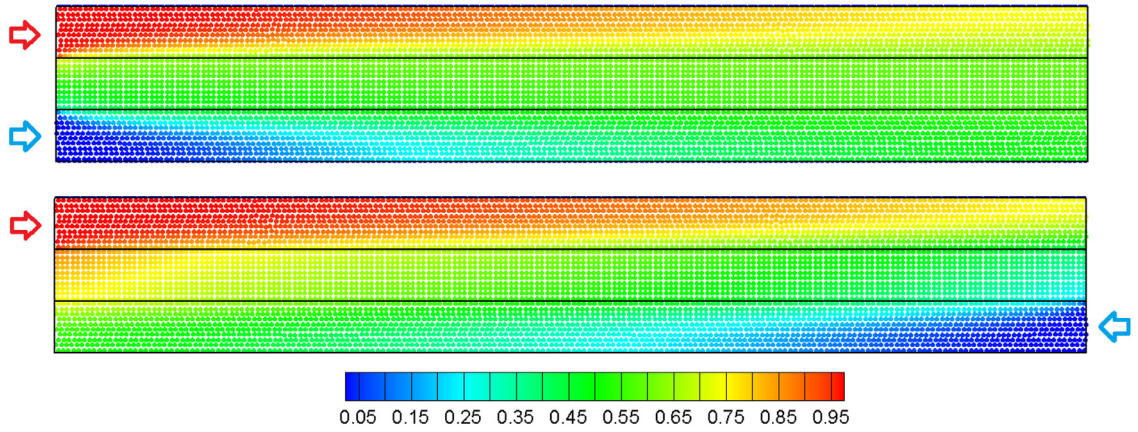

Fig. 22. Dimensionless particle temperature ($T^* = (T\text{-}T_C)/(T_H\text{-}T_C)$) at $t = 2000$ s for parallel-flow (top) and counter-flow (bottom) heat exchangers. Red and blue arrows indicate hot and cold flow inlets, respectively. $T_H = 800$ K and $T_C = 300$ K.

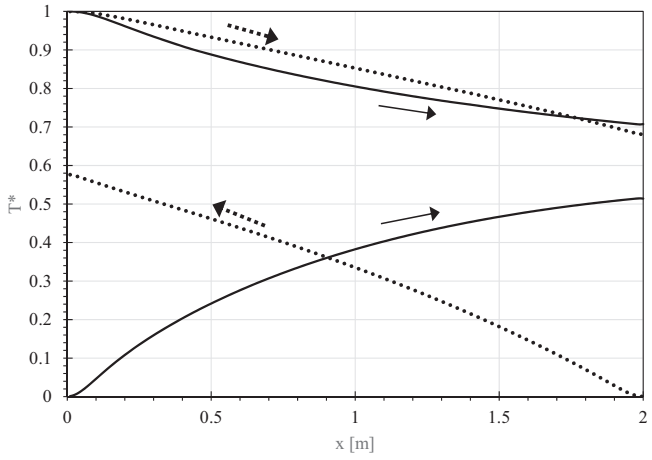

Fig. 23. Streamwise dimensionless temperature ($T^* = (T\text{-}T_C)/(T_H\text{-}T_C)$) distributions along the centrelines of the hot and cold flow streams. Solid line: parallel-flow heat exchanger. Dotted line: counter-flow heat exchanger.

the fluid and solid bodies, the harmonic mean of thermal conductivities has been used. We have applied the above formulation in simulating heat transfer problem in a hydrodynamically fully-developed channel whereby the periodic boundary condition has been used for the hydrodynamic variables. Nevertheless, in order to simulate the thermally-developing flow in the channel, we have relied on the background mesh (used for neighbour searching) to model the Dirichlet inlet temperature boundary condition, without having to build the temperature reset zone at the upstream region of the flow inlet beforehand. For verification purpose, we have tested the SPH solver on simple problems such as solid heat conduction in homogeneous and heterogeneous materials, before applying the solver in simulating more complex problems such as fluid-solid CHT problems in flow channel and heat exchangers. The SPH results have been compared against the analytical and other numerical solutions and good agreement has been found. For all the fluid flow simulations presented in the current work, we have activated the shifting algorithm as we have found that it can promote numerical stability while simulating flow cases of high *Re*.

The current work has presented the fully-coupled approach while solving the energy equations in fluid and solid domains. This approach, however, would be computationally expensive if the time scale disparity between the fluid and solid domains is large. A loosely coupled approach might be more appropriate for practical applications. Also, the implicit time marching scheme could be implemented so that a larger time step size could be employed.

Acknowledgement

The first author would like to thank UNITEN for providing the computing facility during the course of the simulation work.

References

[1] Ng KC, Aziz MAA, Ng EYK. On the effect of turbulent intensity towards the accuracy of the zero-equation turbulence model for indoor airflow application. Build Environ 2011;46:82–8. doi:10.1016/j.buildenv.2010.07.002.
[2] Ahmed MA, Yusoff MZ, Ng KC, Shuaib NH. Numerical investigations on the turbulent forced convection of nanofluids flow in a triangular-corrugated channel. Case Stud Therm Eng 2015;6:212–25. doi:10.1016/j.csite.2015.10.002.
[3] Ng KC, Ng EYK, Yusoff MZ, Lim TK. Applications of high-resolution schemes based on normalized variable formulation for 3D indoor airflow simulations. Int J Numer Methods Eng 2008;73. doi:10.1002/nme.2106.
[4] Li ZX, Zhong TS, Niu JL, Xiao F, Zhang LZ. Conjugate heat and mass transfer in a total heat exchanger with cross-corrugated triangular ducts and one-step made asymmetric membranes. Int J Heat Mass Transf 2015;84:390–400. doi:10.1016/j.ijheatmasstransfer.2015.01.032.
[5] Wang P, Li Y, Zou Z, Zhang W. Conjugate heat transfer investigation of cooled turbine using the preconditioned density-based algorithm. Propuls Power Res 2013;2:56–69. doi:10.1016/j.jppr.2012.10.004.
[6] Horvat A, Catton I. Numerical technique for modeling conjugate heat transfer in an electronic device heat sink. Int J Heat Mass Transf 2003;46:2155–68. doi:10.1016/S0017-9310(02)00532-X.
[7] Pareschi G, Frapolli N, Chikatamarla SS, Karlin I V. Conjugate heat transfer with the entropic lattice Boltzmann method. Phys Rev E 2016;94:013305. doi:10.1103/PhysRevE.94.013305.
[8] Montomoli F, Adami P, Martelli F. A finite-volume method for the conjugate heat transfer in film cooling devices. Proc Inst Mech Eng Part A J Power Energy 2009;223:191–200. doi:10.1243/09576509JPE640.
[9] Monaghan JJ. Smoothed particle hydrodynamics. Annu Rev Astron Astrophys 1992;30:543–74. doi:10.1146/annurev.aa.30.090192.002551.
[10] Liu MB, Liu GR. Smoothed particle hydrodynamics (SPH): an overview and recent developments. Arch Comput Methods Eng 2010;17:25–76. doi:10.1007/s11831-010-9040-7.
[11] Shadloo MS, Oger G, Le Touzé D. Smoothed particle hydrodynamics method for fluid flows, towards industrial applications: motivations, current state, and challenges. Comput Fluids 2016;136:11–34. doi:10.1016/j.compfluid.2016.05.029.
[12] Koshizuka S, Oka Y. Moving-particle semi-implicit method for fragmentation of incompressible fluid. Nucl Sci Eng 1996;123(3):421–34.
[13] Ng KC, Ng EYK, Lam WH. Lagrangian simulation of steady and unsteady laminar mixing by plate impeller in a cylindrical vessel. Ind Eng Chem Res 2013;52. doi:10.1021/ie400621b.
[14] Ng KC, Hwang YH, Sheu TWH, Yu CH. Moving Particle Level-Set (MPLS) method for incompressible multiphase flow computation. Comput Phys Commun 2015;196:317–34. doi:10.1016/j.cpc.2015.06.021.
[15] Ng KC, Hwang YH, Sheu TWH. On the accuracy assessment of Laplacian models in MPS. Comput Phys Commun 2014;185. doi:10.1016/j.cpc.2014.05.012.
[16] Ng KC, Ng YL, Lam WH. Particle simulation and flow sequence on drainage of liquid particles. Comput Math with Appl 2013;66. doi:10.1016/j.camwa.2013.08.018.
[17] Ng KC, Ng EYK. Laminar mixing performances of baffling, shaft eccentricity and unsteady mixing in a cylindrical vessel. Chem Eng Sci 2013;104. doi:10.1016/j.ces.2013.10.031.

[18] Groot RD, Warren PB. Dissipative particle dynamics: bridging the gap between atomistic and mesoscopic simulation. J Chem Phys 1997;107(11):4423–35.
[19] Ng KC, Sheu TWH. Refined energy-conserving dissipative particle dynamics model with temperature-dependent properties and its application in solidification problem. Phys Rev E 2017;96. doi:10.1103/PhysRevE.96.043302.
[20] Zhang YX, Yi HL, Tan HP. A dissipative particle dynamics algorithm for fluid-solid conjugate heat transfer. Int J Heat Mass Transf 2016;103:555–63. doi:10.1016/j.ijheatmasstransfer.2016.07.094.
[21] Monaghan JJ. Simulating free surface flows with SPH. J Comput Phys 1994;110:399–406. doi:10.1006/jcph.1994.1034.
[22] Xu X, Deng XL. An improved weakly compressible SPH method for simulating free surface flows of viscous and viscoelastic fluids. Comput Phys Commun 2016;201:43–62. doi:10.1016/j.cpc.2015.12.016.
[23] Zhang A, Sun P, Ming F, Colagrossi A. Smoothed particle hydrodynamics and its applications in fluid-structure interactions. J Hydrodyn Ser B 2017;29:187–216. doi:10.1016/S1001-6058(16)60730-8.
[24] Nomeritae Daly E, Grimaldi S, Bui HH. Explicit incompressible SPH algorithm for free-surface flow modelling: a comparison with weakly compressible schemes. Adv Water Resour 2016;97:156–67. doi:10.1016/j.advwatres.2016.09.008.
[25] Ullah H, Ullah M, Afridi H, Conci N, De Natale FGB. Traffic accident detection through a hydrodynamic lens. In: Proc. - Int. Conf. Image Process, 2015. ICIP; 2015. p. 2470–4. doi:10.1109/ICIP.2015.7351246.
[26] Elekaei Behjati H, Navvab Kashani M, Biggs MJ. Modelling of immiscible liquid-liquid systems by Smoothed Particle Hydrodynamics. J Colloid Interface Sci 2017;508:567–74. doi:10.1016/j.jcis.2017.08.072.
[27] Yang D, Wu K, Wan L, Sheng Y. A particle element approach for modelling the 3D printing process of fibre reinforced polymer composites. J Manuf Mater Process 2017;1:10. doi:10.3390/jmmp1010010.
[28] Cohen RCZ, Cleary PW, Mason B. Improving understanding of human swimming using smoothed particle hydrodynamics. In: IFMBE Proc., 31. IFMBE; 2010. p. 174–7. doi:10.1007/978-3-642-14515-5_45.
[29] Nasiri H, Abdollahzadeh Jamalabadi MY, Sadeghi R, Safaei MR, Nguyen TK, Safdari Shadloo M. A smoothed particle hydrodynamics approach for numerical simulation of nano-fluid flows: application to forced convection heat transfer over a horizontal cylinder. J Therm Anal Calorim 2018;4:1–9. doi:10.1007/s10973-018-7022-4.
[30] Szewc K, Pozorski J, Tanire A. Modeling of natural convection with smoothed particle hydrodynamics: non-boussinesq formulation. Int J Heat Mass Transf 2011;54:4807–16. doi:10.1016/j.ijheatmasstransfer.2011.06.034.
[31] Feng Z, Ponton MC. Smoothed particle method for studying heat and mass transfer between fluid and solid. In: Proc. ASME 2014 Int. Mech. Eng. Congr. Expo. IMECE2014 Novemb. 14-20, 2014. Montr; 2017. p. 1–7.
[32] Lei JM, Yang H, Huang C. Comparisons among weakly-compressible and incompressible smoothed particle hdrodynamic algorithms for natural convection. Wuli Xuebao/Acta Phys Sin 2014;63:224701. doi:10.7498/aps.63.224701.
[33] Aly AM. Modeling of multi-phase flows and natural convection in a square cavity using an incompressible smoothed particle hydrodynamics. Int J Numer Methods Heat Fluid Flow 2015;25:513–33. doi:10.1108/HFF-05-2014-0161.
[34] Aly AM, Chamkha AJ, Lee S-W, Al-Mudhaf AF. On mixed convection in an inclined lid-driven cavity with sinusoidal heated walls using the ISPH method. Comput Therm Sci 2016;8:337–54. doi:10.1615/ComputThermalScien.2016016527.
[35] Aly AM, Asai M. ISPH method for double-diffusive natural convection under cross-diffusion effects in an anisotropic porous cavity/annulus. Int J Numer Methods Heat Fluid Flow 2016;26:235–68. doi:10.1108/HFF-03-2015-0085.
[36] Nguyen MT, Aly AM, Lee SW. Effect of a wavy interface on the natural convection of a nanofluid in a cavity with a partially layered porous medium using the ISPH method. Numer Heat Transf Part A Appl 2017;72:68–88. doi:10.1080/10407782.2017.1353385.
[37] Nguyen MT, Aly AM, Lee SW. A numerical study on unsteady natural/mixed convection in a cavity with fixed and moving rigid bodies using the ISPH method. Int J Numer Methods Heat Fluid Flow 2018;28:684–703. doi:10.1108/HFF-02-2017-0058.
[38] Jeong JH, Jhon MS, Halow JS, Van Osdol J. Smoothed particle hydrodynamics: applications to heat conduction. Comput Phys Commun 2003;153:71–84. doi:10.1016/S0010-4655(03)00155-3.
[39] Vishwakarma V, Das AK, Das PK. Steady state conduction through 2D irregular bodies by smoothed particle hydrodynamics. Int J Heat Mass Transf 2011;54:314–25. doi:10.1016/j.ijheatmasstransfer.2010.09.040.
[40] Cleary PW, Monaghan JJ. Conduction modelling using smoothed particle hydrodynamics. J Comput Phys 1999;148:227–64. doi:10.1006/jcph.1998.6118.
[41] Trautmann M, Hertel M, Füssel U. Numerical simulation of TIG weld pool dynamics using smoothed particle hydrodynamics. Int J Heat Mass Transf 2017;115:842–53. doi:10.1016/j.ijheatmasstransfer.2017.08.060.
[42] Tarwidi D. Smoothed particle hydrodynamics method for two-dimensional Stefan problem. In: Proceeding Fifth Int. Symp. Comput. Sci.; 2012. p. 34–42.
[43] Cao WJ, Yang DZ, Lu XW, He Y, YZ Z. Numerical simulation of flow and heat transfer during filling process based on SPH method. Adv Mater Res 2013;658:276–80. www.scientific.net/AMR.658.276. doi:10.4028/.
[44] Pan W, Li D, Tartakovsky AM, Ahzi S, Khraisheh M, Khaleel M. A new smoothed particle hydrodynamics non-Newtonian model for friction stir welding: process modeling and simulation of microstructure evolution in a magnesium alloy. Int J Plast 2013;48:189–204. doi:10.1016/j.ijplas.2013.02.013.
[45] Faizal F, Rendian Septiawan R. Computational study on melting process using smoothed particle hydrodynamics. J Mod Phys 2014;5:112–16. doi:10.4236/jmp.2014.53019.
[46] Tong M, Browne DJ. Smoothed particle hydrodynamics modelling of the fluid flow and heat transfer in the weld pool during laser spot welding. IOP Conf Ser Mater Sci Eng 2012;27:012080. doi:10.1088/1757-899X/27/1/012080.
[47] Ryan EM, Tartakovsky AM, Amon C. A novel method for modeling Neumann and Robin boundary conditions in smoothed particle hydrodynamics. Comput Phys Commun 2010;181:2008–23. doi:10.1016/j.cpc.2010.08.022.
[48] Esmaili Sikarudi MA, Nikseresht AH. Neumann and Robin boundary conditions for heat conduction modeling using smoothed particle hydrodynamics. Comput Phys Commun 2016;198:1–11. doi:10.1016/j.cpc.2015.07.004.
[49] Cleary PW. Modelling confined multi-material heat and mass flows using SPH. Appl Math Model 1998;22:981–93. doi:10.1016/S0307-904X(98)10031-8.
[50] Rook R, Yildiz M, Dost S. Modeling transient heat transfer using SPH and implicit time integration. Numer Heat Transf Part B Fundam 2007;51:1–23. doi:10.1080/10407790600762763.
[51] Aly AM, Asai M, Chamkha AJ. Analysis of unsteady mixed convection in lid-driven cavity included circular cylinders motion using an incompressible smoothed particle hydrodynamics method. Int J Numer Methods Heat Fluid Flow 2015;25:2000–21. doi:10.1108/HFF-10-2014-0305.
[52] Ganzenmüller GC, Steinhauser MO, Liedekerke PV. The Implementation of Smoothed Particle Hydrodynamics in LAMMPS; 2011. Retrieved from http://lammps.sandia.gov/doc/USER/sph/SPH_LAMMPS_userguide.pdf.
[53] Sun PN, Colagrossi A, Marrone S, Zhang AM. The δplus-SPH model: simple procedures for a further improvement of the SPH scheme. Comput Methods Appl Mech Eng 2017;315:25–49. doi:10.1016/j.cma.2016.10.028.
[54] Adami S, Hu XY, Adams NA. A generalized wall boundary condition for smoothed particle hydrodynamics. J Comput Phys 2012;231:7057–75. doi:10.1016/j.jcp.2012.05.005.
[55] Mokos A, Rogers BD, Stansby PK. A multi-phase particle shifting algorithm for SPH simulations of violent hydrodynamics with a large number of particles. J Hydraul Res 2017;55:143–62. doi:10.1080/00221686.2016.1212944.
[56] Sun PN, Colagrossi A, Marrone S, Antuono M, Zhang AM. Multi-resolution Delta-plus-SPH with tensile instability control: towards high Reynolds number flows. Comput Phys Commun 2017;224:63–80. doi:10.1016/j.cpc.2017.11.016.
[57] Morris JP. A study of the stability properties of smooth particle hydrodynamics. Publ Astron Soc Aust 1996;13:97–102.
[58] Monaghan JJ. SPH without a tensile instability. J Comput Phys 2000;159:290–311. doi:10.1006/jcph.2000.6439.
[59] Vacondio R, Rogers BD, Stansby PK, Mignosa P, Feldman J. Variable resolution for SPH: a dynamic particle coalescing and splitting scheme. Comput Methods Appl Mech Eng 2013;256:132–48. doi:10.1016/j.cma.2012.12.014.
[60] Basa M, Quinlan NJ, Lastiwka M. Robustness and accuracy of SPH formulations for viscous flow. Int J Numer Methods Fluids 2009;60:1127–48. doi:10.1002/fld.
[61] Meister M, Burger G, Rauch W. On the Reynolds number sensitivity of smoothed particle hydrodynamics. J Hydraul Res 2014;52:824–35. doi:10.1080/00221686.2014.932855.